European Journal of Medicinal Chemistry 82 (2014) 120–126

Contents lists available at ScienceDirect

European Journal of Medicinal Chemistry

journal homepage: http://www.elsevier.com/locate/ejmech

Preliminary communication

Group A streptococcus inhibitors by high-throughput virtual screening

Haipeng Hu [a], Shuli Mao [a], Julia V. Bugrysheva [b,1], Sarah Pruett [c], Dennis C. Liotta [a], June R. Scott [b], James P. Snyder [a,*]

[a] Department of Chemistry, Emory University, 1515 Dickey Drive, Atlanta, GA 30322, USA
[b] Department of Microbiology and Immunology, Emory University School of Medicine, 1510 Clifton Road, Atlanta, GA 30322, USA
[c] Yerkes National Primate Research Center, Emory University, 201 Dowman Drive, Atlanta, GA 30322, USA

ARTICLE INFO

Article history:
Received 15 December 2013
Received in revised form
29 April 2014
Accepted 1 May 2014
Available online 4 May 2014

Keywords:
Group A streptococcus
RNase J1/J2
Homology model
High-throughput virtual screening (HTVS)

ABSTRACT

Group A streptococcus (GAS) is a Gram-positive bacterium, which can cause multiple types of disease from mild infections of skin and throat to invasive and life-threatening infections. Recently RNase J1 and J2 were found to be essential for the growth of GAS. In order to identify inhibitors against RNase J1/J2, homology models of both the ligand-free apo-form and the ligand-bound holo-form complexes were constructed as templates for high-throughput virtual screening (HTVS). A focused small molecule library and the commercially available Maybridge database were employed as sources for potential inhibitors. A cell-based biological assay identified two compounds with 10 μM MIC activity.

© 2014 Elsevier Masson SAS. All rights reserved.

1. Introduction

Streptococcus pyogenes, also known as group A streptococcus (GAS), is a Gram-positive bacterium and one of the most frequent pathogens in humans. It is estimated that about 5–15% of normal individuals harbor the bacterium, usually in the respiratory tract without signs of disease [1]. Most GAS infections are relatively mild illnesses such as streptococcal sore throat (strep throat) or streptococcal skin infections (impetigo). However, GAS can also cause more serious conditions such as scarlet fever, rheumatic fever, postpartum fever, wound infections and pneumonia [2]. Occasionally these bacteria can cause severe and even life-threatening diseases. Termed "invasive GAS disease", the latter occur when bacteria invade parts of the body where they are usually not found, such as the blood, muscle or lungs [3]. Two of the most severe forms of invasive GAS are necrotizing fasciitis and streptococcal toxic shock syndrome. Necrotizing fasciitis, occasionally described by the media as "the flesh-eating bacteria", is a rapidly progressive disease which destroys muscles, fat and skin tissue. On the other hand, streptococcal toxic shock syndrome (STSS) results in a rapid drop in blood pressure as organs such as the kidney, liver and lungs begin to fail. While 10%–15% of untreated patients with invasive GAS disease die from their infection, approximately 25% of patients with necrotizing fasciitis and more than 35% with STSS experience the same fate [3]. Current treatments for GAS include oral or IV injection of antibiotics such as penicillin and surgical removal of dead tissues. Early treatment can reduce the risk of death from invasive disease, but it cannot prevent death in every case. In addition, an increasing number of GAS strains are being reported to show resistance to one or more antibiotics. Although there are no GAS strains resistant to penicillin at present, treatment with this antibiotic fails to eradicate GAS infections in up to a third of all cases [4]. Therefore, the development of new drugs is crucial.

The ability of GAS to produce different diseases and to infect the host results from its ability to regulate expression of virulence factors required for attachment to host tissues, evade the host immune response and spread rapidly throughout the host [5–7]. Because of its importance in disease progression, regulation of gene expression in GAS has been studied, and it is believed that control of mRNA decay is an important mechanism of this regulation. Recently, Bugrysheva and Scott found that RNase J1 and J2 are essential for growth of GAS and play independent roles in mRNA decay of the organism [8]. Therefore, if small molecules can be

* Corresponding author.
E-mail address: jsnyder@emory.edu (J.P. Snyder).
[1] Current address: National Center for Emerging and Zoonotic Infectious Diseases, Centers for Disease Control and Prevention, 1600 Clifton Road NE, MS G-08, Atlanta, GA 30333, USA.

http://dx.doi.org/10.1016/j.ejmech.2014.05.006
0223-5234/© 2014 Elsevier Masson SAS. All rights reserved.

identified to inhibit RNase J1/J2, GAS growth should be terminated. To date, while several strategies for mediating GAS have been described [9–12], attempts to block RNase J1 or J2 have not appeared in the literature.

Since neither crystal structures of RNase J1/J2 in GAS nor known inhibitors of the enzymes had been reported, during the course of our work, we employed two computational tools in an effort to overcome the deficits. The first is homology modeling, in which an atomic-resolution model of the "target" protein is constructed from its amino acid sequence and an experimental three-dimensional structure of a related homologous protein. In this study, we prepared a homology model of GAS RNase J1 based on the X-ray crystal structure of *Thermus thermophilus* RNase J. The second tool is high-throughput virtual screening, in which a large library of drug-like chemicals is screened computationally against the receptor (i.e. homology model) followed by experimental assay of those compounds predicted to bind well. Although the physical screening of chemicals against a biological target is one dominant technique in drug discovery, high-throughput virtual screening has also been shown to be successful in predicting new ligands along with their receptor-bound structures, sometimes with high hit rates [13–15]. Herein, we demonstrate a high-throughput virtual screening approach devoted to identification of RNase J1 inhibitors in GAS.

2. Results and discussion

2.1. RNase J target construction

2.1.1. Analysis of the crystal structure of T. thermophilus RNase J

The crystal structure of *T. thermophilus* RNase J has been reported by de la Sierra-Gallay et al. [16] both as the free enzyme (2.3 Å resolution, PDB (Protein Data Bank) code 3BK1) and as a complex with uridine monophosphate (UMP, 2.1 Å, PDB code 3BK2; Fig. S1a, Supporting Information). Structural analysis indicates that *T. thermophilus* RNase J is composed of three distinct domains: a β-lactamase domain which presents in all metallo-β-lactamases, a β-CASP domain which is found only in the β-CASP subfamily of β-lactamases, and a C-terminal domain which is present only in RNase J orthologues (Fig. S1b, Supporting Information). The enzyme's catalytic center, where RNA is hydrolyzed, is located in the cleft between its β-lactamase and β-CASP domains. The catalytic center is formed by several conserved histidines and aspartic acids that bind two Zn^{2+} cations as in most β-lactamases. In *T. thermophilus* RNase J, Asp172 bridges both Zn^{2+} cations as does a Zn-coordinating water molecule. The latter simultaneously establishes a hydrogen bond with His376. His75, His77 and His150 provide three ligands to Zn-1, while His80, His398 and Asp79 ligate Zn-2. Asp204 maintains the orientation of His376 through a hydrogen bond in a manner similar to the hydrogen bond formed between Asp38 and His80. Within the catalytic center of the free enzyme, a sulfate ion resides in a site identical to that of the phosphate of bound UMP forming either water-bridged or direct hydrogen bond interactions with His372, Ser340, Ser374 and Ser151 (Fig. S1c and S1d in the Supporting Information). For the purpose of coupling the homology models with the accompanying screening strategy (see below), we define this sulfate site together with the catalytic center as the "catalytic center binding pocket".

2.1.2. Sequence alignments

The sequences of GAS RNase J1 and J2 obtained from the NCBI (protein accession numbers: AAM80227.1 and AAM79264.1) contain 560 and 553 amino acids, respectively. They were aligned with the sequence of *T. thermophilus* RNase J using the EBI MUSCLE multi sequence alignment protocol [17]. The alignment is shown in Fig. S2 in the Supporting Information. In this alignment, RNase J1 and J2 of GAS share 39%, 33% identities and 59%, 50% similarities with *T. thermophilus* RNase J. Investigating the alignment further, we found the residues which comprise the catalytic center including histidines 75, 77, 80, 150, 372, 376, 398, aspartates 38, 79, 204, 172 and serines 151, 340, 374 are highly conserved in both RNase J, J1 and J2. The residues are organized into sequence motifs I–VIII. Considering that the proposed ligand binding pocket is deeply buried within the cleft between β-CASP and β-lactamase domains, and all the conserved motifs reside in the β-CASP and β-lactamase domains, the C-terminal domain of RNase J was removed and the remaining sequences were realigned with MUSCLE. With the new sequence alignment, the identities between RNase J1 and RNase J and between RNase J2 and RNase J increased to 44% and 38%, respectively.

2.1.3. Homology models of RNase J1

Homology modeling was performed with MODELLER version 9.1 [18] using both the apo-form (two Zn^{2+} cations and a sulfate in the proposed binding pocket) and the UMP complex holo-form (UMP and two Zn^{2+} cations) of *T. thermophilus* RNase J as templates. Model construction included complete backbone and side chain building, loop building and verification of model quality. The crystallized ligands including Zn^{2+} cations, sulfate and UMP were preserved during homology model construction. However, all water molecules inherited from the crystal structure were removed in order to permit potential inhibitory ligands to coordinate with Zn^{2+} at the catalytic site. Were one to retain these water molecules, including the ones coordinated to the Zinc cation, ligand docking in the vicinity of the metal atoms would be blocked. The stereochemical and energetic parameters of the initial 3D protein models were evaluated by PROCHECK [19] and Protein Report in Maestro [20]. Prime version 2.2 [21] embedded in the Schrodinger Suite was used to optimize loop conformations, side chain rearrangement and the placement of insertions and deletions while respecting the template structure context and conservation of structural features with a functional role. The final model was analyzed a second time with PROCHECK for violations of main chain Phi/Psi dihedral bond angle ratios and backbone/side chain steric conflicts (Table S2, Supporting Information). To verify the accuracy of the binding site of the homology model, the water molecules in the binding pocket of the *T. thermophilus* RNase J crystal structure were merged into the GAS RNase J1 homology model and optimized to avoid conflict with the protein by using Protein Preparation Wizard in the Schrodinger Suite. UMP was docked back into the homology model with Glide 5.6 [22] and superposed with the 3BK2 crystal structure to show that the ligand-bound model binding site and the UMP ligand match with a heavy-atom RMSD = 0.38 Å. It should be noted that for the virtual screening discussed below, the water molecule was removed in the 3D docking step in order to allow potential ligands to coordinate with the zinc cation. Figures were generated using Pymol 0.99rc6 [23].

2.1.4. Structure comparisons

Two homology models were generated for RNase J1: the apo-form with two Zn^{2+} cations and a sulfate in the proposed binding pocket and the holo-form complex including UMP and two Zn^{2+} cations. For RNase J1, the root mean square (RMS) deviation between the backbone atoms of the two models and their corresponding templates are both less than 0.4 Å (Fig. 1a and b). In both models, conformations of the His and Asp side chains around the Zn^{2+} cations are highly conserved. Due to the absence of water molecules in the homology model, each Zn^{2+} is surrounded by 4 ligands. An exception is the second zinc cation in the holo-form model that exhibits tri-coordination resulting from side chain flipping of Asp80 [24] (Fig. 2a).

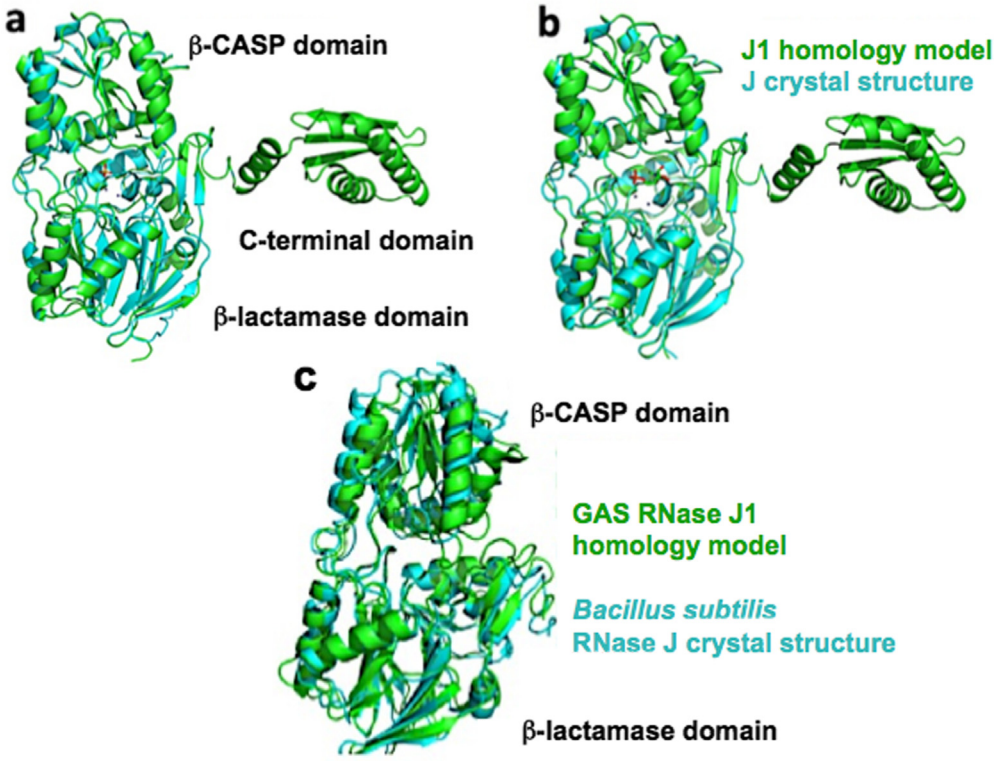

Fig. 1. a) Superposition of the apo-form of GAS RNase J1 homology model with RNase J crystal structure. b) Superposition of the holo-form of RNase J1 homology model with the RNase J crystal structure. c) Superposition of the holo-form of GAS RNase J1 homology model with the crystal structure of *Bacillus subtilis* RNase J1.

In this dehydrated model of GAS RNase J1, the carboxyl side chain of Asp80 bends close to the uridine ring of UMP and forms an alternative hydrogen bond with it. In addition, the hydrogen bonds between His376 and Asp204, His80 and Asp38 in the crystal structure [25] of *T. thermophilis* RNase J survive in both homology models. At the anion binding site, the sulfate ion in the apo-form and the phosphate moiety of UMP occupy the same locus as in the crystal structure. Both functionalities form hydrogen bonds with His366 and Ser344. Unlike the crystal structure, the side chain of Ser374 rotates 75° away from the sulfate group leading to loss of an H-bond with the OH that is replaced by a new hydrogen bond with the corresponding backbone nitrogen. For Ser151, due to the absence of a water molecule, the water-bridged H-bond interaction is missing in the homology model causing the side chain to rotate 120° away from the catalytic center (Fig. 2b).

A recently reported crystal structure of RNase J1 from *B. subtilis* (3.0 Å resolution, PDB code 3ZQ4 [26], Fig. 1c) was also compared with the holo-form of the GAS RNas J1 homology model derived from *T. thermophilus* RNase J. It shares a higher sequence identity with GAS RNase J1 than the latter template, but was not employed for homology modeling in the present work because of its lower 3.0 Å resolution (*vs.* 2.1 and 2.3 Å for *T. thermophiles*).

Consistently, the *B. subtilis* structure delivers a 2.2 Å overall RMSD when compared with the GAS RNase J1 homology model, which drops to 0.74 Å if only the residues around the UMP ligand are considered. The same comparison between the GAS RNase J1

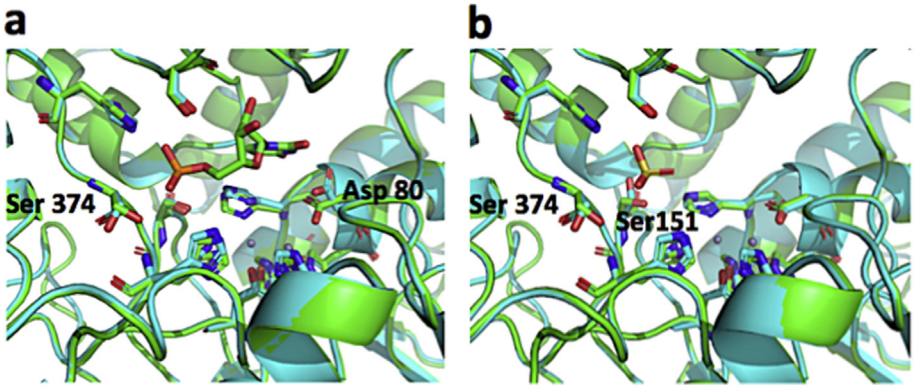

Fig. 2. a) Superposition of the catalytic center of the holo-form of GAS RNase J1 (cyan) with *T. thermophilis* RNase J crystal structure (green). b) Superposition of catalytic center of the apo-form of GAS RNase J1 (cyan) with *T. thermophilis* RNase J (green). (For interpretation of the references to colour in this figure legend, the reader is referred to the web version of this article.)

homology models and the corresponding templates provides 0.42 and 0.39 Å RMSD values, reinforcing the highly conserved nature of the catalytic center. The two Zn^{2+} ions are coordinated by five His and two Asp residues, while Asp78 (corresponding to Asp79 in the *T. thermophilus* RNase J template) presents a conformation similar to that in the ligand-free *T. thermophilus* apo-form (3BK1).

2.2. High-throughput virtual screening (HTVS)

2.2.1. High-throughput virtual screening of a focused library

Construction of the focused library was based on consideration of the nature of the catalytic center of RNase J1. The latter suggests two distinct molecular classes: analogs of the UMP prodrug (Fig. 3) and variations of known β-lactamase inhibitors compatible with the β-lactamase-like binding site (Fig. 4). Both classes were used for thirteen separate similarity searches with ChemNavigator [27] based on the individual structures of Figs. 3 and 4.

For the first class, since the X-ray crystal structure of *T. thermophilus* RNase J complexed with UMP is known, a small molecule that can mimic UMP is likely to be able to compete with RNA hydrolysis and inhibit the function of RNase J1.

However, UMP can pass the cell membrane only with difficulty because of its negatively charged phosphate group. Therefore, similar structures based on a prodrug form were sought as templates to establish the library, anticipating that a monophosphate could be generated in the cell after prodrug hydrolysis and thereby block the function of RNase J1 upon binding. Unfortunately, no such molecules are commercially available. In addition, several selected nucleoside analogs were tested, but none of them showed activity below 50 μM. At this point, we turned our attention to the second larger class of β-lactamase inhibitors. Since RNase J1 contains a β-lactamase domain, the catalytic center of which resembles that of metallo-β-lactamases, screening of the Protein Data Bank [28] for metallo-β-lactamases complexed with an inhibitor was performed. Twelve metallo-β-lactamase inhibitors were collected and used as templates for similarity searches to generate a focused library containing 2609 compounds. By using the high-throughput virtual screening strategy depicted in Fig. 5, the top ten compounds with the highest affinity Glide docking scores in the GAS RNase J1 homology model were identified and acquired. All of them contain a carboxylic acid moiety presumed to replace the crystallized water and bridge the two zinc cations at the binding site. However, none of the substances showed any inhibition of GAS growth at 50 μM in the cell-based screen.

2.2.2. High-throughput virtual screening of the general library

Since inhibitors based on UMP prodrug and β-lactamase templates could not be identified within ChemNavigator, we searched for potential ligand binding sites in other clefts found in the homology model. Five such pockets (I to V, Fig. 6) were identified with CASTp [29]. Pocket I is a hydrophilic space that sits between the β-lactamase and β-CASP domains surrounded by helices α2, α4 and α7. Pocket II is also located between the same two domains. Compared with pocket I and the catalytic binding center, P-II is narrower and more polar being surrounded by Asp176, Tyr273, Glu148 and Lys141. Pocket III is hydrophobic, deeply buried within the β-lactamase domain and sandwiched between two β-sheet layers. Pocket IV sits above β3 and β5 and is sandwiched by α1 and α2. This pocket is hydrophilic on the α2 side but more hydrophobic on the α1 side. Pocket V is a small hydrophobic pocket above the β-CASP domain between the β-sheet layer and α9. Compared with the surroundings of the proposed catalytic center, all five accessory pockets are smaller, but still reasonably sized for ligand binding (from 372 to 862 Å [3]). To this end, we employed the Maybridge HitFinder Collection [30], which comprises drug-like compounds extracted from the Maybridge Screening Collection by clustering with the standard Daylight Fingerprints algorithm and filtered by Lipinski guidelines.

With the high-throughput virtual screening workflow shown in Figure 5, 13,000 compounds were obtained from the Maybridge collection following solubility and membrane permeability filtering. Subsequent docking into the six pockets described above provided 60 compounds selected for biological screening. Of these, 38 were located in the catalytic binding pocket, 5 each from pockets I, III, IV, V and 2 from pocket II. The compounds were tested in the cell-based GAS growth assay resulting in two hits: **18** and **8** at 10 and 50 μM from pockets IV and I, respectively. Using the compounds as templates, a specific focused library was generated by ChemNavigator similarity and substructure searches. Members of this new library were docked into their respective pockets of origin. The top 23 compounds, including ten analogs of **8**, ten analogs of **18** and three precursors of **18**, were acquired for the follow-up biological screen resulting in five compounds which inhibit the growth of GAS below 50 μM (see Table 1). Among them, four new hits (**78**, **82**–**84**) are analogs of **18**, which contain an aromatic imine moiety with a hydroxyl group in the *ortho*-position. The fifth hit is **85**, a precursor aldehyde of **18** (see Table S1 in the Supporting Information for vender ID).

Further investigation of **18** and its five active analogs by a higher precision docking protocol, Glide extra precision docking, suggests that the aromatic imine moiety locates at the bottom of pocket IV surrounded by hydrophobic residues Ile37, Ile62, Val69, Leu72, Leu89, Ile94. Docked **18** is shown as an example in Fig. 7. Additional predicted binding poses of the other compounds and their superposition are depicted in Fig. S3a–f in the Supporting Information. A hydrogen bond between the *ortho*-hydroxyl oxygen and the residues at the end of α2 is consistently observed. The other terminus of these compounds extends into the region between the β4 β-sheet and the α2 helix and forms a hydrogen bond with Phe87 at the end of α2. Compound **82** with two aromatic imine groups linked by a cyclohexane ring is the exception. One of its aromatic imine groups resides in the same site as the other active analogs, while the second distal aromatic imine extends into solvent, and its OH group forms a hydrogen bond with Phe87.

While it is encouraging that the hit imines are active, it is also known that this functional group is susceptible to degradation in

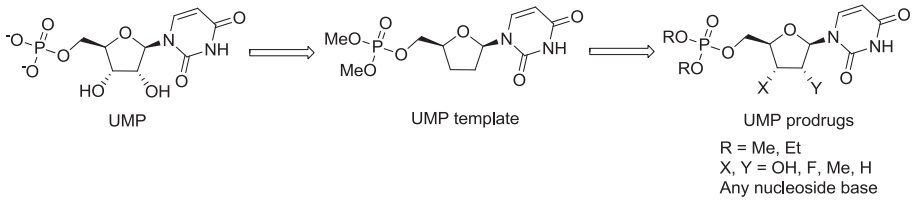

Fig. 3. Structures of UMP template and UMP prodrugs.

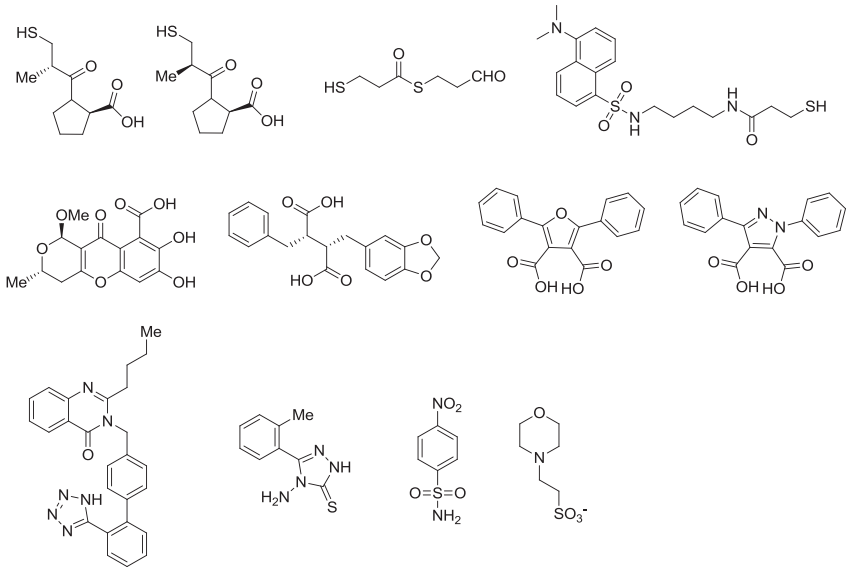

Fig. 4. Known β-lactamase inhibitors used for similarity searches.

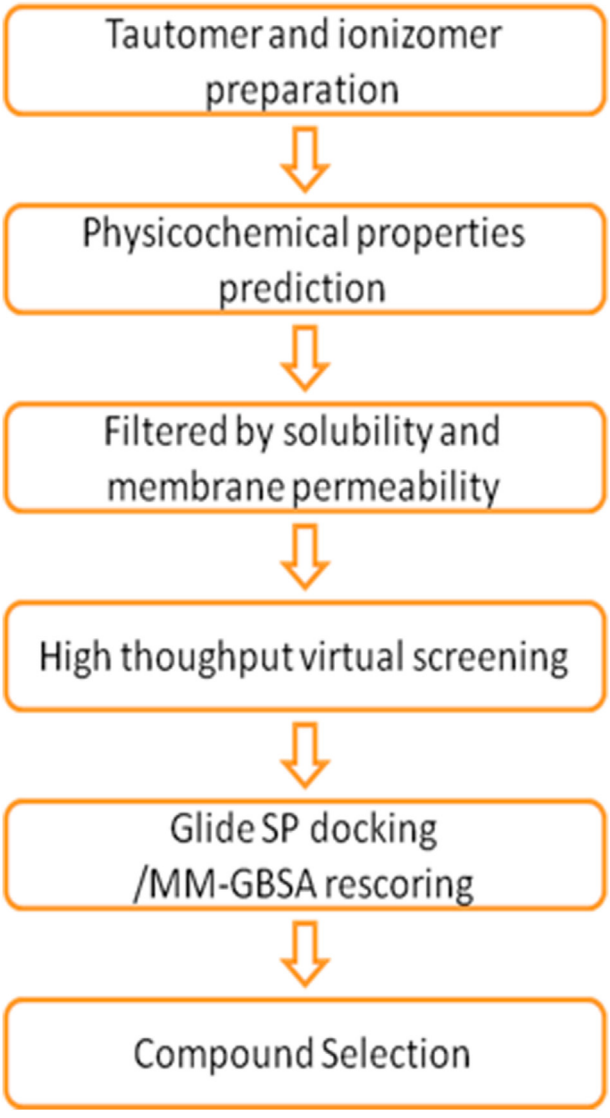

Fig. 5. High-throughput virtual screening workflow for focused and general libraries.

aqueous medium. Such compounds are easily hydrolyzed to give the corresponding aldehyde and amine, although aromatic imines are somewhat more stable than aliphatic imines due to conjugation. In order to test the stability of **18** and **82** in water, LC-MS analysis was employed. After 2 h of dissolution in water, both compounds exhibited the amine fragments from hydrolysis, although the corresponding aldehydes were not detected. The processes continued smoothly over a 4 h monitoring period (See Supporting Information for details). While we have not investigated the decomposition products further, it is clear that the current hit compounds need synthetic modification to improve both potency and aqueous stability.

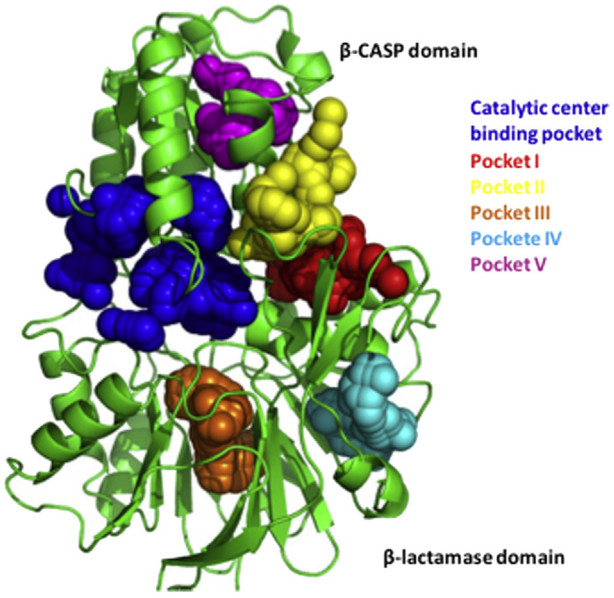

Fig. 6. Catalytic center binding pocket (blue) and five other possible pockets I–V. (For interpretation of the references to colour in this figure legend, the reader is referred to the web version of this article.)

Table 1
Seven compounds inhibit GAS growth with MIC below 50 μM.

Compound no.	Structure	Inhibition concentration
18	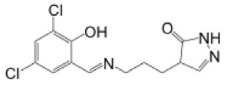	10 μM
82	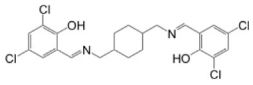	10 μM
83	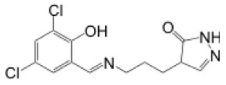	20 μM
84	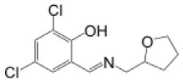	20 μM
85	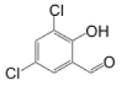	20 μM
78	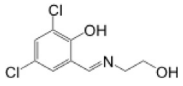	40 μM
8	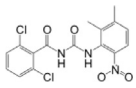	50 μM

3. Conclusions

In this work, we have assumed that RNase J1 and J2 are meaningful targets for management of Group A streptococcus (GAS) bacteria and the more virulent variation termed "invasive GAS disease" responsible for a number of life-threatening infections such as toxic shock syndrome. Given that penicillin is still commonly used for control of GAS, while more modern antibiotics are resistance prone, our preliminary goal has been to develop a strategy for identifying a new generation of potentially developable anti-GAS agents. Accordingly, we have demonstrated that homology modeling in combination with high-throughput virtual screening can be used successfully to recognize GAS inhibitors with no prior information regarding ligands that bind to RNase J1/J2. Among 93 compounds extracted by HTVS from a large database and tested, seven showed 10–50 μM inhibition activity of GAS growth for a hit rate of 7.5%. The 10 μM value is in the same range as employed for other antibiotics such as chloramphenicol [31–33]. Since the aromatic imine hits evidence low tolerability in water, the series requires optimization before it can be regarded as providing genuine leads. An attractive next step could involve lead hopping with **18** and **82** as templates by means of approaches such as that provided by OpenEye [34,35]. One caveat to the work concerns target validation. Our assay is cell based; thus, the specific target proteins have yet to be determined. Expression of RNase J1 and J2 and the development of reliable in vitro assays will be necessary to verify that these proteins are primarily responsible for the anti-GAS action of the compounds in Table 1.

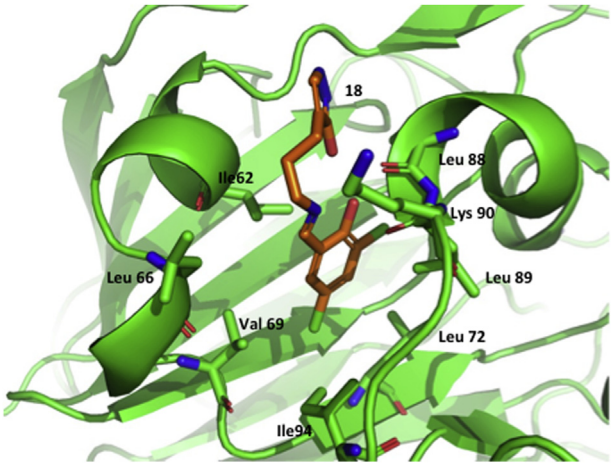

Fig. 7. Binding pose and interactions of **18** with Ile62, Val69, Leu72, Leu89 and Ile94 in pocket IV.

4. Experimental

4.1. High-throughput virtual screening strategy

High-throughput virtual screening was performed against both the holo and apo RNase J1 homology models with two separate libraries, namely a focused library containing 2609 compounds generated by similarity searching from ChemNavigator for small molecules related to the RNase J catalytic center binding pocket and a larger general library named Maybridge HitFinder Collection which is composed by 14,400 drug-like compounds obtained from Maybridge Screening Collection by clustering with standard Daylight Fingerprints algorithm and filtered by Lipinski guidelines. For each library, a high-throughput virtual screening workflow was performed as illustrated by Fig. 5.

First, the tautomers and ionization states of library members were generated with LigPrep version 2.4 [36]. Then QikProp version 3.3 [37] was used to predict the physicochemical properties of each compound. The corresponding aqueous solubilities and membrane permeabilities were utilized to filter the compound libraries through the LigFilter application in Maestro [20] in order to retain only those structures with predicted drug-like properties. HTVS (high-throughput virtual screening) using VSW (virtual screening workflow) [38] was performed with the filtered libraries, and the top 10% of the compounds were selected for a greater precision docking study with Glide followed by MM/GBSA rescoring by Prime. Top compounds in the final list were acquired for the cell-based biological assay.

4.2. Characterization of library compounds and hits

Screening compounds for the general library were purchased from both Maybridge (81 compounds) and Princeton BioMolecular Research (2 compounds). Focused library members were purchased from Princeton BioMolecular Research (10 compounds). According to the suppliers' quality control specifications, all 93 compounds ordered from both suppliers were greater than 90% pure as established by ^{1}H NMR and/or LC-MS with a majority of compounds having a purity of 95% [30,39].

4.3. Cell-based biological activity

Compounds were dissolved in DMSO to 10 mM and diluted with THY (Todd Hewitt medium with 0.2% yeast extract) prior mixing with bacteria. Bacterial cells of the GAS strain MGAS2221 grown overnight in 3 mL THY at 37 °C were vortexed for 10 s to break chains and subsequently diluted to 2–4 x 10^{6} colony forming unit (cfu)/mL with THY. Bacterial numbers were determined by

microscope counts and confirmed by plating on THY agar plates. Compounds and cells were mixed and incubated in 96 well plates in the microplate reader for 12 h at 37 °C. The GAS growth in each well of the 96-well plate was followed by measuring OD600 every 30 min. Each compound was tested in this growth assay in duplicate with MIC concentrations of 10–50 μM as reported in Table 1.

Acknowledgements

We are grateful to Open Eye Scientific Software for generous provision of software enabling scaffold hopping and other molecular design tasks.

Appendix A. Supplementary data

Supplementary data related to this article can be found at http://dx.doi.org/10.1016/j.ejmech.2014.05.006.

References

[1] a) A.L. Roberts, K.L. Connolly, D.J. Kirse, A.K. Evans, K.A. Poehling, T.R. Peters, S.D. Reid, BMC. Pediatr. 12 (2012) 3;
b) http://www.textbookofbacteriology.net/streptococcus.html; (accessed 12.15.13.).
[2] http://en.wikipedia.org/wiki/Group_A_streptococcal_infection; (accessed 12.15.13.).
[3] a) A.C. Steer, T. Lamagni, N. Curtis, J.R. Carapetis, Drugs 72 (2012) 1213–1227;
b) J.A. Al-ajmi, P. Hill, C. O'Boyle, M.L. Garcia, M. Malkawi, A. George, F. Saleh, B. Lukose, B.A. Ali, M. Elsheikh, J. Infect. Public Health 5 (2012) 388–393;
c) http://www.cdc.gov/ncidod/dbmd/diseaseinfo/groupastreptococcal_g.htm; (accessed 12.15.13.).
[4] E.L. Kaplan, D.R. Johnson, Pediatrics 108 (2001) 1180–1186.
[5] G. Churchward, Mol. Microbiol. 64 (2007) 34–41.
[6] I. Gryllos, R. Grifantini, A. Colaprico, S. Jiang, E. Deforce, A. Hakansson, et al., Mol. Microbiol. 65 (2007) 671–683.
[7] E.R. Hondorp, K.S. Mclver, Mol. Microbiol. 66 (2007) 1056–1065.
[8] J.V. Bugrysheva, J.R. Scott, Mol. Microbiol. 75 (2010) 731–743.
[9] B.D. Yestrepsky, Y. Xu, M.E. Breen, X. Li, W.G. Rajeswaran, J.G. Ryu, R.J. Sorenson, Y. Tsume, M.W. Wilson, W. Zhang, D. Sun, H. Sun, S.D. Larsen, Bioorg. Med. Chem. 21 (2013) 1880–1897.
[10] A. Sharma, D.K. Aarya, V. Sagar, R. Bergmann, G.S. Chhatwal, A.K. John, J. Proteome Res. 12 (2013) 336–346.
[11] N. Tsap, C.-F. Kuo, H.-Y. Lei, K.-J. Huang, J. App. Microbiol. 108 (2010) 936–944.
[12] I.A. Critchley, U.A. Ochsner, Curr. Opin. Chem. Biol. 12 (2008) 409–417.
[13] B.K. Shoichet, Nature 432 (2004) 862–865.
[14] M.S. Schapira, B.M. Raaka, S. Das, L. Fan, M. Totrov, Z. Zhou, S.R. Wilson, R. Abagyan, H.H. Samuels, Proc. Nat. Acad. Sci. 100 (2003) 7354–7359.
[15] A. Evers, G. Klebe, J. Med. Chem. 47 (2004) 5381–5392.
[16] I.L. De la Sierra-Gallay, L. Zig, A. Jamalli, H. Putzer, Nat. Struct. Mol. Biol. 15 (2008) 206–212.
[17] R.C. Edgar, Nucl. Acids Res. 32 (2004) 1792–1797.
[18] A. Šali, T.L. Blundell, J. Mol. Biol. 234 (1993) 779–815.
[19] R.A. Laskowski, M.W. Macarthur, D.S. Moss, J.M. Thornton, J. Appl. Cryst. 26 (1993) 283–291.
[20] Maestro, Version 9.2, Schrödinger, LLC, New York, NY, 2011.
[21] Prime, Version 2.2, Schrödinger, LLC, New York, NY, 2010.
[22] Glide, Version 5.6, Schrödinger, LLC, New York, NY, 2010.
[23] The PyMOL Molecular Graphics System, Version 0.99rc6, Schrödinger, LLC.
[24] The Corresponding Residue Number in the Crystal Structure is Asp79.
[25] His370 and Asp197, His81 and Asp39 in the Corresponding Homology model.
[26] J.A. Newman, L. Hewitt, C. Rodrigues, A. Solovyova, C.R. Harwood, R.J. Lewis, Structure 19 (2011) 1241.
[27] ChemNavigator, 10919 Technology Place, Suite B, San Diego, CA 92127, U.S.A. http://www.chemnavigator.com/ (accessed 12.15.13.).
[28] F.C. Bernstein, T.F. Koetzle, G.J. Williams, E.E. Meyer Jr., M.D. Brice, J.R. Rodgers, O. Kennard, T. Shimanouchi, M. Tasumi, J. Mol. Biol. 112 (1977) 535.
[29] J. Dundas, Z. Ouyang, J. Tseng, A. Binkowski, Y. Turpaz, J. Liang, Nucl. Acids Res. 34 (2006) W116–W118.
[30] Fisher Scientific USA, 2000. Park Lane Drive, Pittsburgh, PA 15275–1126, http://www.maybridge.com/ (accessed 12.15.13.).
[31] V. Rocco, G. Overturf, Antimicrob. Agents Chemother. (1982) 349–351.
[32] S. Mandal, M.D. Mandal, N.K. Pal, J. Med. Sci. 58 (2004) 16–23.
[33] T. Nagabhushan, G.H. Miller, K.J. Varma, Offprints from Kirk-othmer: Encyclopedia of Chemical Technology, fourth ed., vol. 2, John Wiley and Sons, Inc, New York, 1992, pp. 961–978.
[34] a) P.C.D. Hawkins, A.G. Skillman, A. Nicholls, Comparison of shape-matching and docking as virtual screening tools, J. Med. Chem. 50 (2007) 74–82;
b) J. Venhorst, S. Nunez, J.W. Terpstra, C.G. Kruse, J. Med. Chem. 51 (2008) 3222–3229;
c) R.P. Sheridan, G.B. McGaughey, W.D. Cornell, J. Comput.-Aided Molec. Des. 22 (2008) 257–265.
[35] a) P.C.D. Hawkins, A.G. Skillman, G.L. Warren, B.A. Ellingson, M.T. Stahl, J. Chem. Inf. Model. 50 (2010) 572–584;
b) P.C.D. Hawkins, A. Nicholls, J. Chem. Inf. Model. 52 (2012) 2919.
[36] LigPrep, Version 2.4, Schrödinger, LLC, New York, NY, 2010.
[37] QikProp, Version 3.3, Schrödinger, LLC, New York, NY, 2010.
[38] Schrödinger Suite 2010 Virtual Screening Workflow; Glide Version 5.6, Schrödinger, LLC, New York, NY, 2010. LigPrep version 2.4, Schrödinger, LLC, New York, NY, 2010; QikProp Version 3.3, Schrödinger, LLC, New York, NY, 2010.
[39] http://www.princetonbio.com/pages16.html; (accessed 12.15.13.).